

Ru@MIL-125/MnO_x metal-organic-framework-based cocatalysts for photocatalytic nitrogen fixation

Chuanjiao Wang^a, Shuo Wang^a, Yi Ping^a, Zhe Zhao^a, Dongxue Guo^b, Danhong Wang^{a,b,*}, Xianhe Bu^{a,b}

^a TKL of Metal and Molecule Based Material Chemistry, School of Materials Science and Engineering, Nankai University, Tianjin 300350, China

^b Frontiers Science Center for New Organic Matter, College of Chemistry, Nankai University, Tianjin 300350, China



ARTICLE INFO

Keywords:

Ru nanoparticles
MnO_x
MOF-based cocatalysts
Photocatalytic nitrogen fixation

ABSTRACT

Efficient separation and utilization of photogenerated carriers are critical factors in photocatalysis. Herein, it is proved that cocatalyst with separated oxidation and reduction active sites enhances the separation of photogenerated carriers and surface photocatalytic activity. NH₂-MIL-125 loaded with Ru nanoparticles is synthesized by hydrothermal method and combined with MnO_x by photodeposition to obtain composite catalyst Ru@MIL-125/MnO_x. By this combination, the photocatalytic nitrogen fixation activity improves by about 10 times compared with untreated NH₂-MIL-125. Ru@MIL-125/MnO_x also shows higher oxygen evolution reaction (OER) activity after the introducing of MnO_x. According to the characterization results, MnO_x can be used as the active center of OER and can catch holes, and Ru is the reaction site of photocatalytic nitrogen reduction and can catch electrons, which promotes the transfer of photogenerated electrons and holes to Ru and MnO_x respectively and reduces the recombination of electrons and holes effectively. Furthermore, Ru@MIL-125/MnO_x facilitates photocatalytic nitrogen fixation in the absence of sacrificial agents, thereby demonstrating its potential application of MOF-based cocatalysts for photocatalytic nitrogen fixation.

1. Introduction

Ammonia is an important chemical product in the world every year [1]. Ammonia plays an irreplaceable role in energy, chemical industry and other pillar industries. Nowadays, the main synthesis method is Haber-Bosch process. The large-scale synthesis of ammonia by the Haber-Bosch process is considered as one of the greatest scientific discoveries of the 20th century. However, the Haber-Bosch process requires high temperatures and pressures of nitrogen and hydrogen for the synthesis of ammonia. In order to get the high temperature (400–500 °C) and high pressure (15–30 MPa) required for the reaction conditions, a large amount of energy is consumed, and about 2% of the Earth's total energy consumption is used to synthesize ammonia every year. At the same time, a large amount of greenhouse gases is discharged during this process, causing serious environmental problems. In order to solve this problem, finding a new clean and efficient method to replace the Haber-Bosch process has become a focus of attention [2–5].

Photocatalysis is considered as one of the directions to solve

environmental problems because the energy required is solar energy and the product is clean [6–8]. Photocatalytic nitrogen fixation is regarded as an alternative to the Haber-Bosch method and has become a hot research direction in recent years [9]. Photocatalysis converts solar energy directly into chemical energy and turns nitrogen and water into ammonia. Since the reaction takes place at room temperature and atmospheric pressure, it is considered as the most ideal method for ammonia synthesis. Photocatalytic nitrogen fixation process includes the efficiency of light capture, photogenerated carrier separation and surface catalytic reaction. At present, low utilization of visible light, severe photogenerated carrier recombination and high N≡N triple bond energy are the three key problems limiting the low ammonia yield of photocatalytic nitrogen fixation reaction. The efficient light absorption, effective carrier separation and surface-catalyzed reaction are the key factors to improve the efficiency of photocatalytic nitrogen fixation.

As a kind of porous crystal materials connected by metal nodes and organic ligands, metal-organic framework materials (MOFs) are widely applied in the realm of catalysis due to their advantages of high specific

* Corresponding author at: TKL of Metal and Molecule Based Material Chemistry, School of Materials Science and Engineering, Nankai University, Tianjin 300350, China.

E-mail address: dhwang@nankai.edu.cn (D. Wang).

surface, special pore structure and adjustability [10,11]. Since most of MOFs have semiconductor properties, the researchers have tried to apply MOFs in the field of photocatalysis [12–16]. MOFs also show great potential in the field of photocatalytic nitrogen fixation [17,18]. Thanks to the high porosity, MOFs can adsorb N₂ dissolved in water, and the distance between N₂ and the catalytic site is shortened, thus contributing to the photocatalytic nitrogen fixation reaction [19–22]. However, although relevant research has made some progress, the application of MOFs in photocatalytic nitrogen fixation is still far from practical application.

The introduction of transition metals is an effective measure to improve the application of MOF materials in the field of photocatalysis, commonly used are Pt, Pd, Rh, Ru, etc. Ru shows excellent photocatalytic activity among the transition metal catalysts studied, and has been further studied in the field of photocatalytic nitrogen fixation [23–26]. The above-mentioned MOFs themselves have high surface area, which is conducive to the dispersion of Ru nanoparticles as reduction co-catalysts in catalytic reactions. Moreover, Ru has a lower N₂ reduction potential than Fe, which is considered to be a better catalyst for nitrogen fixation reaction [27]. Ru-based catalysts are also called the second generation ammonia synthesis catalysts because Fe-based catalysts are the traditional catalysts for nitrogen fixation reaction. Transition metal oxides such as MnO_x [28–30], CoO_x [31] and CuO_x [32] show good catalytic activity in degradation of organic and inorganic pollutants, among which Mn-based oxides are widely used as cocatalysts in the field of photocatalytic oxidation reactions due to its advantages of high oxidation ability. As a semiconductor material, manganese oxide has a narrow band gap, so it can absorb light over a very wide range of frequencies, which is one of the ideal catalysts for photocatalysis [33–35].

To achieve the optimization of MOF photocatalysts with both nitrogen reduction and OER activities using spatially separated Ru and MnO_x as cocatalysts, we design and synthesize Ru@NH₂-MIL-125/MnO_x composite. This composite is constructed by the addition of Ru nanoparticles (NPs) and photodeposition loading of MnO_x on the surface of

nanosized NH₂-MIL-125, which was applied to the photocatalytic nitrogen fixation reaction. We found that the composite catalyst showed nitrogen reduction ability on Ru nanoparticle and water oxidation activity on MnO_x, thus showing synergistic effect. Through detailed structural characterization and other tests, the energy band structure of the composite catalyst was analyzed, and the mechanism of photocatalytic enhancement of nitrogen fixation activity was explained (Scheme 1).

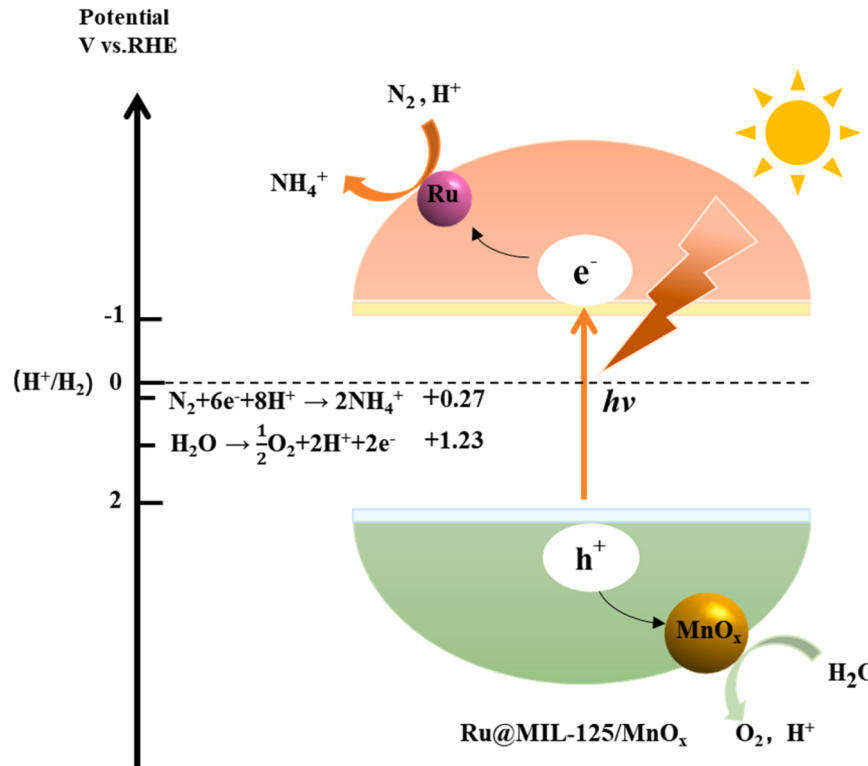
2. Experimental and computational section

2.1. Synthesis of NH₂-MIL-125

NH₂-MIL-125 was synthesized according to the previous report [36–38]. First, 0.543 g 2-amino terephthalic acid (NH₂-BDC) and 0.498 g of terephthalic acid (BDC) were mixed in 20 mL DMF. The mixture was stirred under 300 r min⁻¹ for 0.5 h, after that 0.9 mL of isopropyl titanate was added to the mixture and stirred for 0.5 h, after which 2.2 mL of methanol was added to the mixture. Subsequently, the mixture was transferred to a Teflon lined autoclave and kept at 130 °C for 12 h. Finally, the solution was washed three times with DMF and methanol, respectively. Then drying in vacuum at 60 °C overnight, the NH₂-MIL-125 was obtained.

2.2. Synthesis of Ru@MIL-125

Mixing CTAB, ethanol and water into a solution in a weight ratio of 5:4.5:0.5. 10 g of the above solution was added 0.11 g RuCl₃, and then the mixture was ultrasound to mix evenly, which was denoted as solution A. After that, 0.065 g KBH₄ was added to 10 g solution A, then a frothing substance was observed. Add hot water and repeat centrifugation until there was no floating foam. The solid obtained was Ru nanoparticle. In the process of synthesis of NH₂-MIL-125, 1.8 mL Ru nanoparticle solution was added at the same time when isopropyl titanate was added, then follow the above synthesis steps of NH₂-MIL-125 to



Scheme 1. Diagram of photocatalytic nitrogen fixation reaction mechanism.

continue the synthesis, the Ru@MIL-125 was obtained.

2.3. Synthesis of Ru@MIL-125/MnO_x

0.1 g Ru@MIL-125 catalyst, 0.1 g MnSO₄ and 100 mL water were placed in a glass vessel. After the mixture was irradiated by a 300 W Xe arc lamp with a 400 nm filter for 1 h with stirring. The reactant was washed with water and dried overnight. The powder obtained was Ru@MIL-125/MnO_x.

2.4. Photocatalytic nitrogen fixation reaction

The photocatalytic experiments were conducted in photocatalytic reactor (CEL-APR100H) under illuminating by 300 W Xe lamp (CEL-HXF300). The result was measured by the indophenol blue method combined with the intensity of 655 nm of an ultraviolet spectrophotometer (KU-T6PC). Firstly, 10 mg photocatalyst was dissolved into 50 mL ultrapure water with ultrasonic treatment for 10 min to uniformly disperse. After that, the solution was transferred into a reactor. Secondly, the solution was bubbled in continuously with N₂ at a flow rate of 60–80 mL/min for 0.5 h and then stirring for 0.5 h to reach N₂-saturated solution. The reactor keeps the temperature at 25 °C by circulating condensed water and holds magnetic stirring under illuminating by Xe lamp with a cut-off filter (420 nm) for 2 h. Before irradiation, 2 mL solution was extracted as the blank sample. Then ¹⁵N isotope labeling experiments were performed to confirm that the production of NH₄⁺ was from N₂ reduction, and then liquid chromatography-mass spectrometry (Waters, XEVO TQ-S) was used to analyze the ¹⁵N-labeled product.

2.5. Apparent quantum efficiency (AQE) measurements

$$\text{AQE} = \frac{\text{Ne}}{\text{Np}} \times 100\% = 3 \frac{\text{N}_{\text{NH}_3}}{\text{Np}} = 3 \frac{\text{N}_A n_{\text{NH}_3}}{WAt/(hv)} \times 100\%$$

Where n_{NH₃}, N_p, Ne represent numbers of the generated NH₃, the incident photons, and total number of electrons transferred by the reaction, respectively; W, A and t represent the light intensity, irradiation area and time, respectively; v represents the light frequency; h is Planck constant; N_A is the Avogadro's constant.

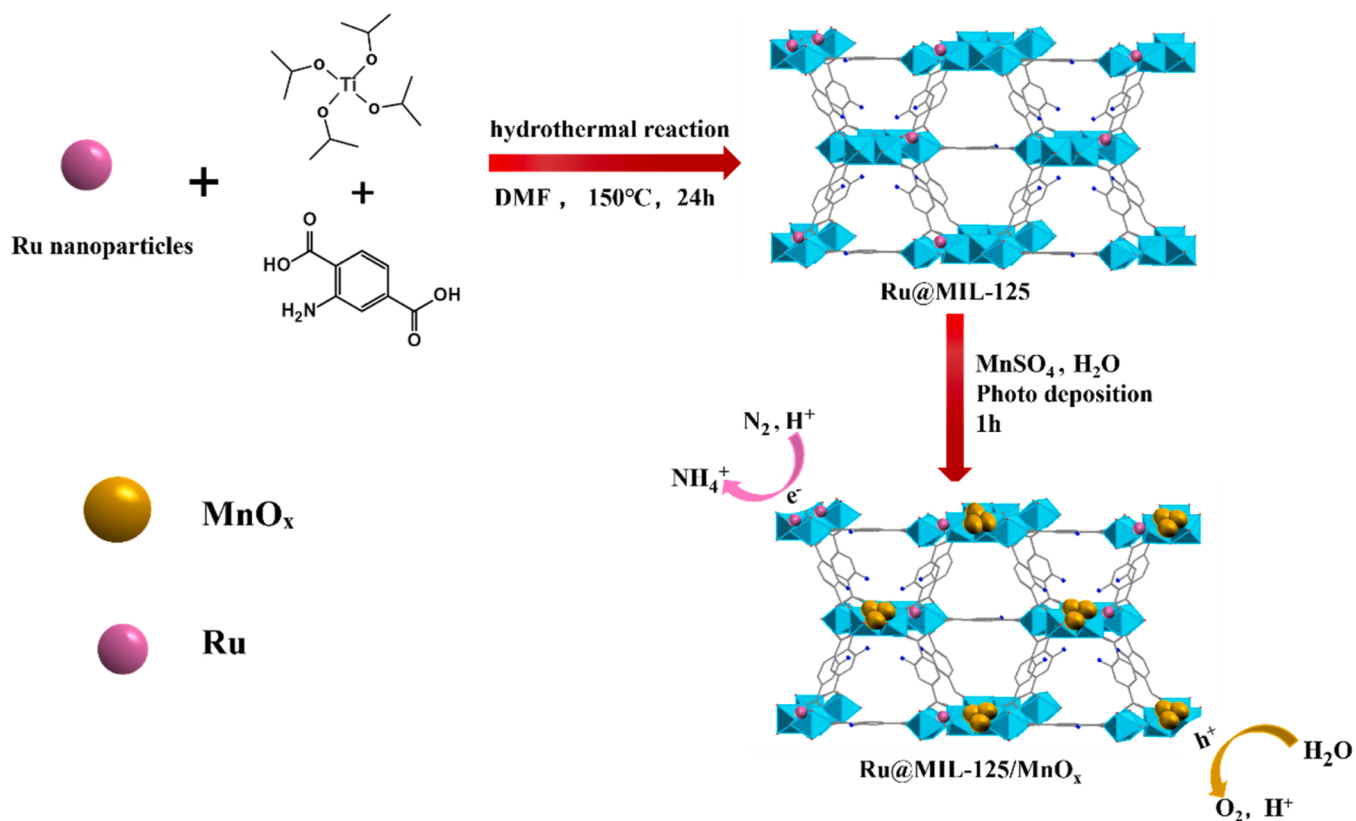
2.6. Computational method

The Vienna Ab Initio Package (VASP) and the generalized gradient approximation (GGA) using the PBE formulation to support all the density functional theory (DFT) calculations [39–41]. Partial occupancies of the Kohn–Sham orbitals were allowed using the Gaussian smearing method and a width of 0.05 eV. A geometry optimization was considered convergent when the force change was smaller than 0.02 eV/Å [42]. Model 1 is a Ru single atom adsorbed onto a typical MIL-125(Ti) cluster in a cubic, periodic box of 20 Å. Model 2 is a Mn₁₀O₂ cluster adsorbed onto a typical MIL-125(Ti) cluster in a cubic, periodic box of 20 Å. During structural optimizations, the Γ point in the Brillouin zone was used for k-point sampling, and all atoms were allowed to relax.

3. Results and discussion

3.1. Preparation and characterization

The preparation of Ru@MIL-125/MnO_x bifunctional photocatalyst is straightforwardly shown in Scheme 2. First, Ru nanoparticles are synthesized, then mixed with NH₂-BDC ligand and isopropyl titanate in DMF solution, and Ru@MIL-125 are thus obtained under solvothermal



Scheme 2. Systematic diagram for the fabrication of Ru@MIL-125/MnO_x cocatalyst for photocatalytic nitrogen fixation.

conditions. Finally, Ru@MIL-125/MnO_x were prepared by photo-deposition of MnO_x. The formular of NH₂-MIL-125 is Ti₈O₈(μ₂-OH)₄(C₆H₃C₂O₄NH₂)₆. The SBU of Ti₈O₈(OH)₄ consists eight edge- and corner-sharing TiO₅(OH) octahedra and is connected by NH₂-BDC ligands. There are two types of cavities as tetrahedral and octahedral shape in NH₂-MIL-125, their effective accessible diameters are 12.55 and 6.13 Å, respectively. When metal particles/metal oxides with high intrinsic photocatalytic activity were supported on NH₂-MIL-125, the strong metal-support interaction has not to date been fully studied. Thus, this work aims to elucidate the microstructure and electronic structure of Ru@MIL-125/MnO_x cocatalyst with both N₂ reduction and OER catalytic activity.

The morphology of the catalysts was revealed by Spherical aberration-corrected TEM, transmission electron microscope (TEM) and scanning electron microscope (SEM) as shown in Fig. 1 and Fig. S1. Ru nanoparticles with a size of about 5 nm ($d_{101} = 0.2058$ nm) and MnO_x nanoparticles with a size of about 5 nm ($d = 0.3349$ nm) were detected in the cocatalysts. MIL-125 shows regular polyhedra with a smooth surface. After Ru loading and MnO_x deposition the surface of polyhedra become rougher for the corrosion. The morphology corrosion for Ru@MIL-125/MnO_x is the most serious compared with Ru@MIL-125 and MIL-125/MnO_x. On the one hand, it can be seen from the EDS elemental mapping images that Ru element is uniformly distributed in both Ru@MIL-125 and Ru@MIL-125/MnO_x particles with a size of about 500 nm, which indicates that Ru exists in the form of separate quantum dots instead of agglomeration. It also shows that the distribution of Mn element in the EDS elemental mapping images for Ru@MIL-125/MnO_x is uniform, so it can be concluded that MnO_x is also uniformly deposited in MIL-125. Line profile along with the blue transverse line further shows the uniform dispersion of Ru and Mn element in MIL-125 polyhedra for Ru@MIL-125/MnO_x.

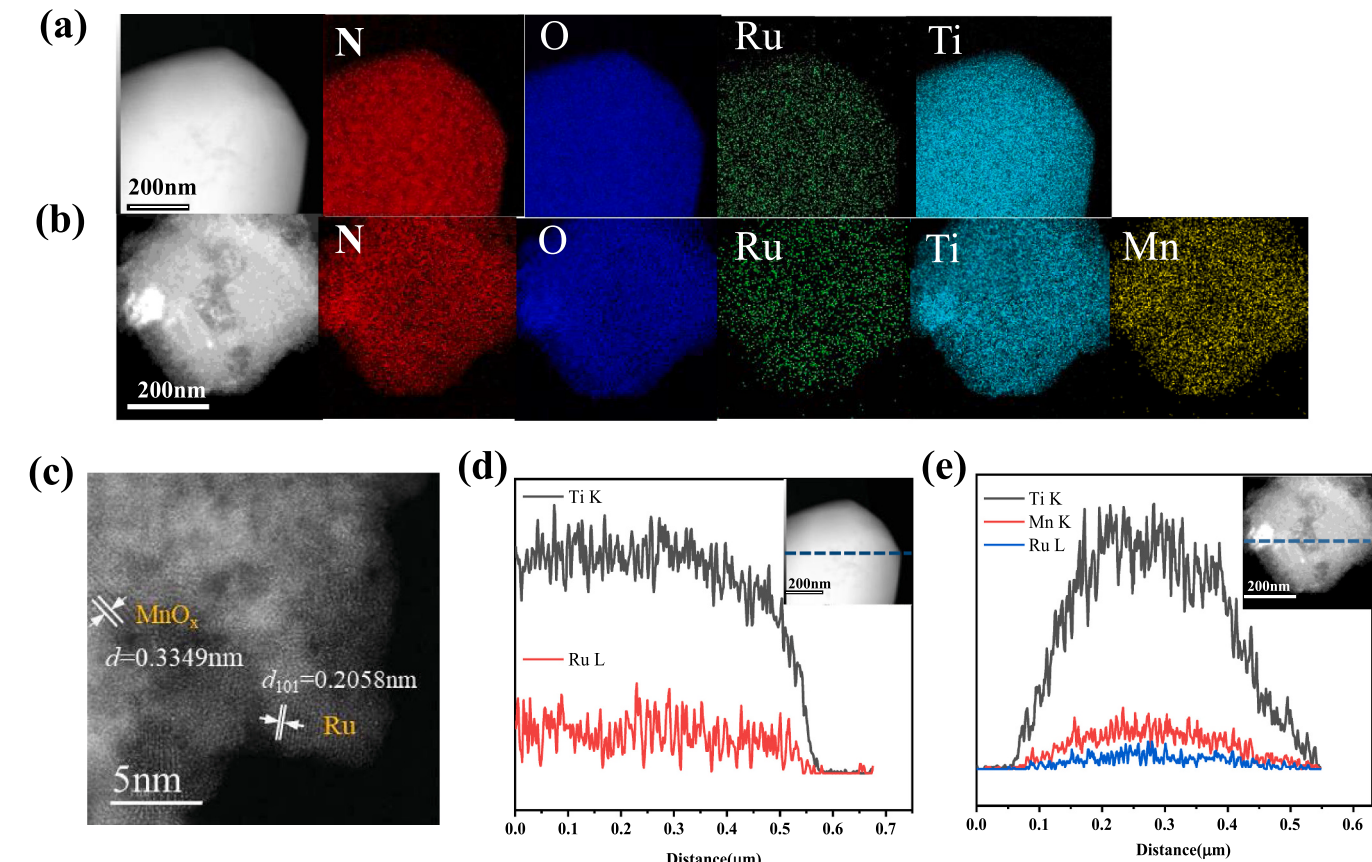


Fig. 1. TEM images and EDS mapping of (a) Ru@MIL-125, (b) Ru@MIL-125/MnO_x, (c)Spherical aberration-corrected TEM images of Ru@MIL-125/MnO_x and line profile along with the blue transverse line of (d) Ru@MIL-125, (e) Ru@MIL-125/MnO_x.

Thermogravimetric analysis was performed for each sample under Ar atmosphere. The results obtained were shown in Fig. S2. After Ru loading and MnO_x deposition, Ru@MIL-125/MnO_x shows the highest residual mass. The inductively coupled plasma (ICP) (Table S1) result certified that the mass fractions of Ti, Mn and Ru for Ru@MIL-125/MnO_x were 14.8%, 2.93% and 2.52%, respectively. The Ti content is very near to the calculated 23.2% from the formular of NH₂-MIL-125 with Ti₈O₈(μ₂-OH)₄(C₆H₃C₂O₄NH₂)₆. The BET surface area and pore volume for Ru@MIL-125/MnO_x decreased due to Ru loading and MnO_x deposition compared with those for NH₂-MIL-125 as shown in Table S2 and Fig. S3. The micropore size of pure NH₂-MIL-125 is calculated to be around 4–8 Å, which is very consistent with the simulated 6.13 Å. Obvious mesopore with a size of 3.94 nm was observed for Ru@MIL-125/MnO_x, which results from Ru loading and MnO_x deposition.

In order to further explore the structure of materials, powder XRD patterns, FT-IR spectra and ¹H/¹³C solid-state NMR spectra of the samples was performed. The results of powder XRD are shown in Fig. 2a. The diffraction peaks of MIL-125, Ru@MIL-125, MIL-125/MnO_x and Ru@MIL-125/MnO_x both show clear and high peak intensity, indicating that the samples synthesized have good crystallinity. According to previous reports[43–45], peaks at 2θ= 6.7°, 9.7° and 11.6° are characteristic of MIL-125 corresponding to the (101), (200), (211) crystal planes, respectively, indicating the successful synthesis of NH₂-MIL-125 material. Ru@MIL-125, MIL-125/MnO_x and Ru@MIL-125/MnO_x exhibit diffraction peaks similar to those of pure NH₂-MIL-125, and no other new peaks appear, which indicates that the structure of NH₂-MIL-125 is not changed in the composite catalysts.

Through infrared detection of the four catalysts prepared (Fig. 2b), the four catalysts all exhibit characteristic peaks at 3346 and 3443 cm⁻¹, which are related to the N-H stretching vibrations in the structural -NH₂ group in NH₂-MIL-125[43,46]. The peak at 1580 cm⁻¹ belongs to the

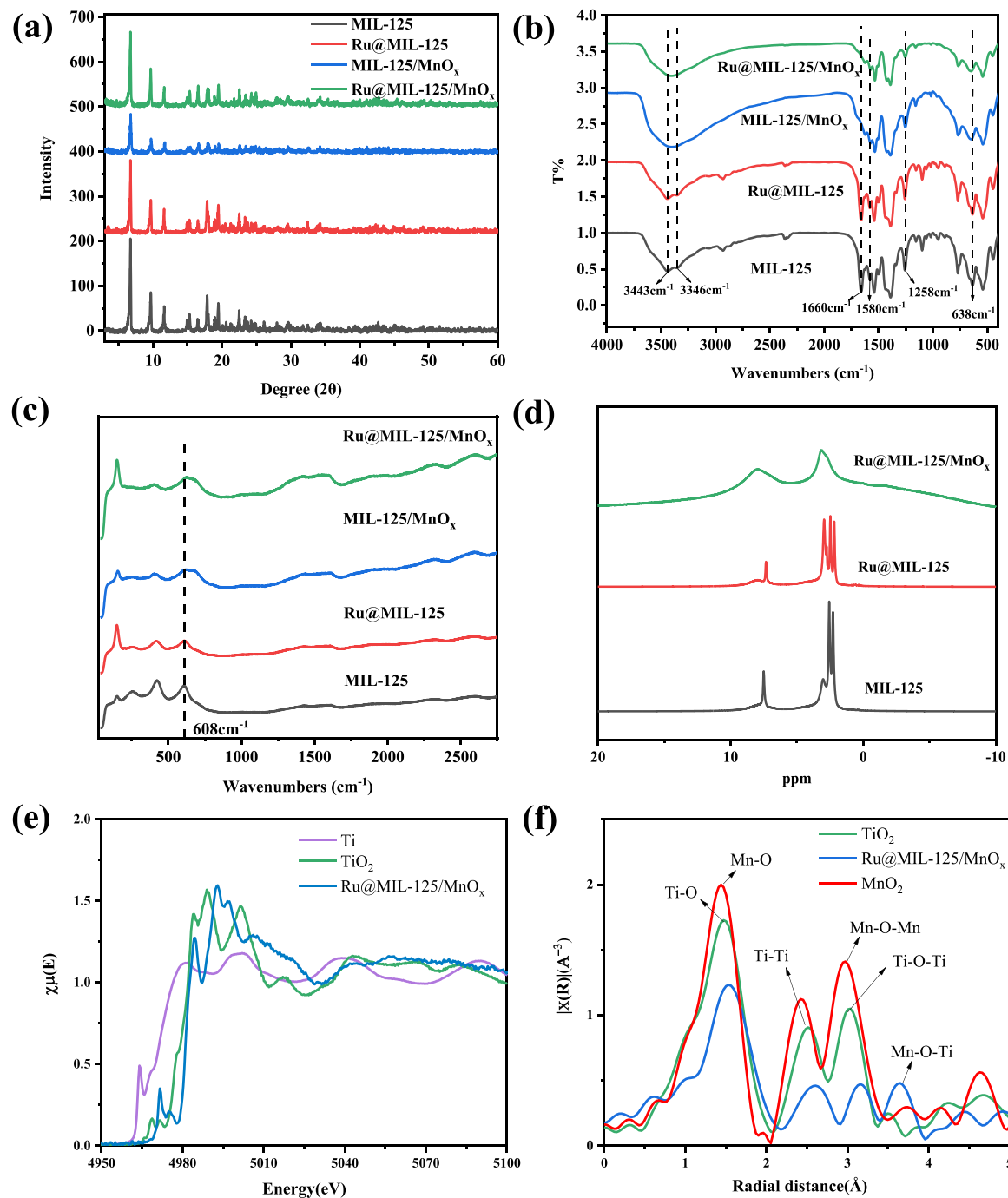


Fig. 2. (a) Powder XRD spectrum, (b) FT-IR spectrum, (c) Raman spectra, (d) ^1H Solid-State NMR spectra, (e) Enlarged X-ray absorption near edge structure (XANES) spectra of Ti K-edge, (f) Extended X-ray absorption fine structure (EXAFS) spectra of Ti K-edge.

in-plane bending vibration of N-H [47,48], and the peak at 1258 cm^{-1} belongs to the C-N stretching vibration [49]. The asymmetric and symmetric stretching vibration of C-O bond in the COO^- carboxylate for $\text{NH}_2\text{-MIL-125}$ are located at 1540 cm^{-1} and 1430 cm^{-1} [48]. The peak at 1660 cm^{-1} in $\text{NH}_2\text{-MIL-125}$ and Ru@MIL-125 is observed [50], which results from characteristic C=O stretching vibration of residual DMF solvents in the samples. However, after the combination with MnO_x , the DMF peak in the $\text{MIL-125}/\text{MnO}_x$ and $\text{Ru@MIL-125}/\text{MnO}_x$ disappears, implying that MnO_x replaced the adsorption position of solvent DMF. Notably, the peak at 638 cm^{-1} belonging to TiO_6 octahedron obviously blue-shifted to 650 cm^{-1} after depositing MnO_x in $\text{NH}_2\text{-MIL-125}$ [51,52], indicating the formation of Mn-O-Ti bond.

In Raman spectra (Fig. 2c), $\text{NH}_2\text{-MIL-125}$ and Ru@MIL-125 both

show a peak at 608 cm^{-1} , which was assigned to Ti-O bond. After depositing MnO_x , $\text{MIL-125}/\text{MnO}_x$ and $\text{Ru@MIL-125}/\text{MnO}_x$ show a blue shift of this peak and a broaden peak at 670 cm^{-1} was observed, which further proves the formation of Mn-O-Ti bond.

Further analysis was conducted by ^1H and ^{13}C NMR spectroscopy, as shown in Fig. 2d and Fig. S4. For ^1H NMR spectra, the peak at 7.5 ppm is related to aromatic H in benzene ring, the peak at 3 ppm is attributed to -NH₂ group, the sharp peaks at 2.4 ppm and 2.1 ppm are assigned to methyl group in DMF solvent adsorbed in $\text{NH}_2\text{-MIL-125}$. After MnO_x deposition, the peaks of methyl group disappear, also implying that MnO_x replaced the adsorbed solvent DMF. For ^{13}C NMR spectra, it can be seen that similar peaks of C are observed in MIL-125 and Ru@MIL-125 . The peaks around $120\text{--}140\text{ ppm}$, 175 ppm and 150 ppm are

attributed to aromatic C and carboxyl C, C-N in NH₂-MIL-125, respectively. The sharp peaks at 30 and 163 ppm are attributed to DMF. Moreover, the split of ¹H peaks disappeared for Ru@MIL-125/MnO_x. It is suggested that the chemical environment of H in MIL-125 changes with the addition of Ru and MnO_x.

To verify the formation of Mn-O-Ti bond in Ru@MIL-125/MnO_x, we performed X-ray absorption fine structure (XAFS) measurements of Ti K-edge. Fig. 2e shows the XANES curves of Ru@MIL-125/MnO_x, metallic Ti and TiO₂ at the Ti k-edge. As expected, the absorption edge of Ru@MIL-125/MnO_x is lower than TiO₂, which indicates that the Ti valence state of Ru@MIL-125/MnO_x is higher than that of TiO₂. This result is consistent with the XPS result that the BE of Ti in Ru@MIL-125/MnO_x shifts to higher side than that in MIL-125. As shown in Fig. 2f, intense peaks at 0.8–2.0 Å assigned to Ti-O bond are observed. The peaks observed at 2.0–4.0 Å are ascribable to Ti-Ti and Ti-O-Ti interactions. The peak at 3.7 Å for Ru@MIL-125/MnO_x is clearly different from that for TiO₂ and MnO₂, which can be attributed for the formation of Mn-O-Ti bond [53]. The results of the wavelet transforms (WT) are consistent with EXAFS spectra (Fig. S5a–c). The Ru@MIL-125/MnO_x exhibits Ti-O bond at 1.5 Å, and the intensity of the Ru@MIL-125/MnO_x near 3–4 Å is higher than the 0–2 Å, which may be caused by the Ti-O-Ti and Ti-O-Mn bonds.

3.2. Electrochemical performance

In order to further investigate the ability of carrier separation and transfer for Ru@MIL-125/MnO_x, visible light photocurrent, visible light EIS curve, CV and Mott–Schottky tests were conducted on all samples. As shown in Fig. 3a, loading MnO_x reduces the impedance of MIL-125.

Ru@MIL-125/MnO_x has the lowest impedance of all the samples. A lower impedance indicates that the sample has a lower resistance of charge transfer. A similar conclusion can be found in the visible light photocurrent test (Fig. 3b), MIL-125 and Ru@MIL-125 samples have almost no photocurrent, while the photocurrent response is significantly enhanced after MnO_x is loaded. Ru@MIL-125/MnO_x composite catalyst has the highest photocurrent response, which illustrates that the addition of Ru and MnO_x contributes to the mobility and the separation of photogenerated carrier, and further increases the number of photo-generated carriers, which is conducive to the improvement of photocatalytic performance. Therefore, the composite Ru@MIL-125/MnO_x may have better photocatalytic properties than the pure MOF.

The Mott–Schottky (MS) curve reflected the Schottky barrier between the semiconductor material and the electrolyte. As shown in Fig. 3c, the type of semiconductor material can be judged by the positive or negative slope of MS curve. The slopes of MIL-125, Ru@MIL-125, MIL-125/MnO_x, Ru@MIL-125/MnO_x samples in this test were all positive, indicating that these samples are n-type semiconductors. The slope of the curve is negatively correlated with the carrier concentration, that is to say, the higher the slope of the MS curve, the lower the carrier concentration. Ru@MIL-125/MnO_x has the smallest slope, which is significantly lower than other samples, showing that this sample has the highest carrier concentration. The slopes of Ru@MIL-125 and MIL-125/MnO_x are smaller than those of MIL-125 samples, concluding that loading Ru or MnO_x is able to increase the carrier concentration because charge transferring to Ru and MnO_x can decrease the recombination of carriers. Besides, the horizontal intercept of MS curve corresponded to the flat band potential of the semiconductor, which is equal to the Fermi level. The calculated flat band potential of MIL-125 and MIL-125/MnO_x

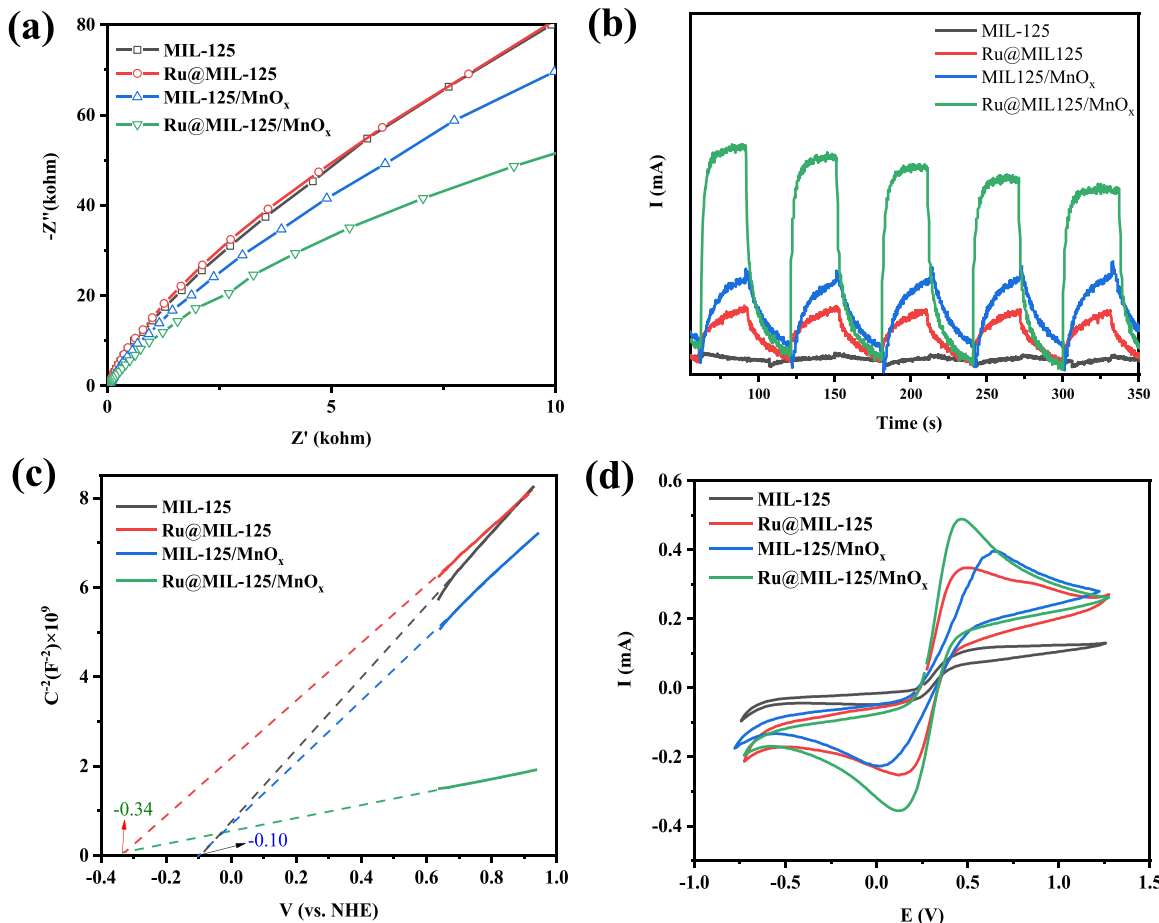


Fig. 3. (a) EIS resistance of MIL-125, Ru@MIL-125, MIL-125/MnO_x, Ru@MIL-125/MnO_x, (b) visible light photocurrent, (c) Mott–Schottky curves, (d) Cyclic voltammetry curves.

are -0.10 V, and the calculated flat band potential of Ru@MIL-125 and Ru@MIL-125/MnO_x are -0.34 V. This result indicates that introducing MnO_x will not affect the Fermi level of NH₂-MIL-125, while introducing Ru will raise the Fermi level of NH₂-MIL-125. Fig. 3d shows the cyclic voltammetry curves of the samples. It can be seen that Ru@MIL-125/MnO_x has the strongest redox capacity and is more likely to have superior photocatalytic nitrogen fixation activity.

3.3. Photocatalytic Nitrogen Fixation mechanism investigation

In order to determine the chemical state of each element in Ru@MIL-125/MnO_x, X-ray photoelectron spectroscopy (XPS) of the sample was performed. As shown in Fig. 4a-f. The C 1 s spectrum has two characteristic binding energy (BE) peaks at 284.8 eV and 288.9 eV, corresponding to C-C and COOR, respectively. While the BE of N 1 s at 399.3 eV for -NH₂ group shifts to higher BE after introducing Ru and MnO_x for Ru@MIL-125/MnO_x. The BE of N1s at 402.7 eV is related to protonated amino group -NH₃⁺ in NH₂-MIL-125(Ti) [54]. The BE of Ti 2p also shifts to higher BE for Ru@MIL-125/MnO_x. These results suggest that NH₂-MIL-125 lose electrons after introducing Ru and MnO_x in the composite. The BE of O 1 s at 530.2 eV is assigned to MnO_x. For O 1 s and Mn 2p, the BEs of Ru@MIL-125/MnO_x shift towards the higher BE, indicating that MnO_x also loses electrons when deposited in Ru@MIL-125. In Ru 3d, Ru^{δ+} at 281 eV and Ru⁰ at 280.5 eV are observed in Ru@MIL-125 and Ru@MIL-125/MnO_x. It can be observed that Ru@MIL-125/MnO_x possesses more Ru⁰ compared with Ru@MIL-125. This result indicates that Ru gains more electrons in Ru@MIL-125/MnO_x composite. Ru may be the nitrogen reduction center in the nitrogen fixation reaction. High electron density on Ru atom will enhance nitrogen reduction activity. According to literature reports, MnO_x may be the active center of oxygen production in the reaction. The separation of oxygen-producing and nitrogen-reducing centers indicates that electrons and holes transfer to different parts, which can significantly lower the recombination of carrier, and then further enhance the nitrogen fixation activity [55,56].

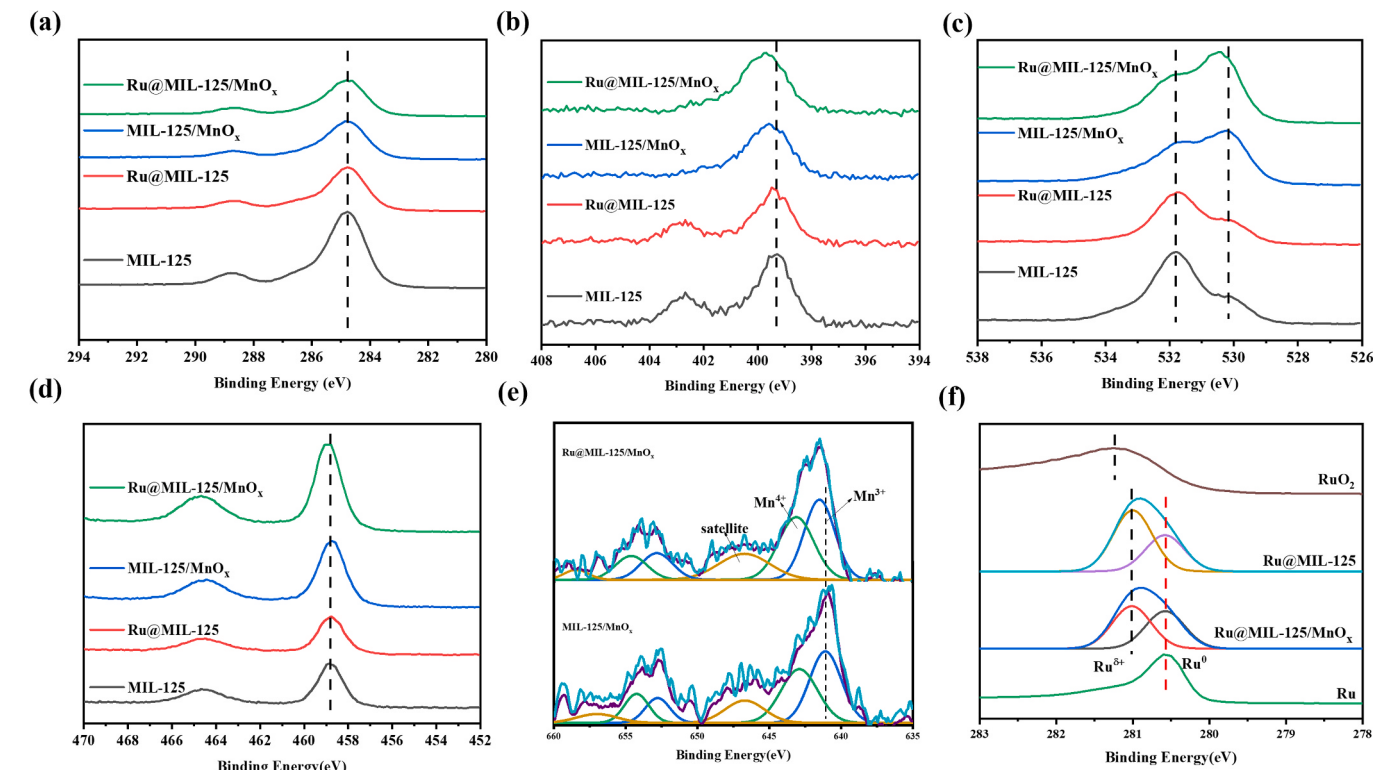


Fig. 4. The XPS photoelectron spectrum of the four catalysts (a) C 1 s, (b) N 1 s, (c) O 1 s, (d) Ti 2p, (e) Mn 2 p, (f) Ru 3d.

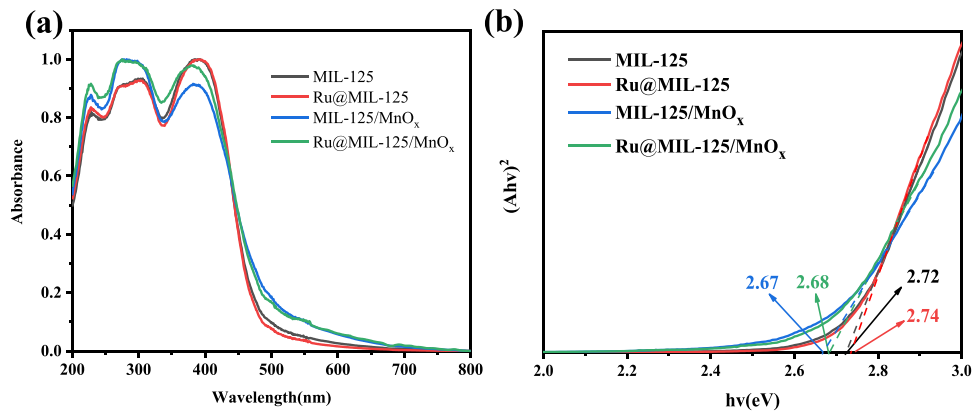


Fig. 5. (a) UV–vis DRS spectra, (b) Kubelka-Munk diagram of the absorption spectrum conversion from UV-Vis DRS.

0.81 eV, 0.23 eV, 0.42 eV and 0.21 eV. After introducing Ru and MnO_x, both the VB and the CB shifted to high level compared with pure NH₂-MIL-125. Pure Ru⁰ shows a Fermi level of -0.18 eV, which is higher than the CB of pure NH₂-MIL-125 (0.81 eV), and is also higher than the reaction potential for nitrogen reduction (0.27 V vs. RHE). So it is suggested nitrogen can obtain the electrons on Ru active sites and be reduced to NH₄⁺. MnO_x semiconductor (Figs. S8 and S9) shows a VB of 1.32 eV, which is lower than the reaction potential for oxygen evolution reaction (OER, 1.23 V vs. RHE). Thus, MnO_x is suggested as the OER active sites.

Through the above data, the energy level diagram of each sample can be obtained, as shown in Fig. 6a. It can be found that the VB of Ru@MIL-

125/MnO_x has slightly increased. Fig. 6b shows the results of transient fluorescence lifetime test. The fluorescence lifetime of MIL-125, Ru@MIL-125, MIL-125/MnO_x and Ru@MIL-125/MnO_x are 0.701 ns, 1.053 ns, 0.648 ns and 0.887 ns, respectively. The results show that Ru can increase the lifetime of photogenerated carriers, while the combination MnO_x is able to shorten the lifetime of carriers. The long lifetime after introducing Ru may be attributed to the fact that the Fermi level of Ru (-0.18 eV) is higher than the VB of MIL-125 as obtained above. In general, Ru@MIL-125/MnO_x has a longer fluorescence lifetime than MIL-125, which is more conducive to photogenerated carrier separation, thus improving the photocatalytic activity of the catalyst.

The steady-state fluorescence test results of the materials are shown

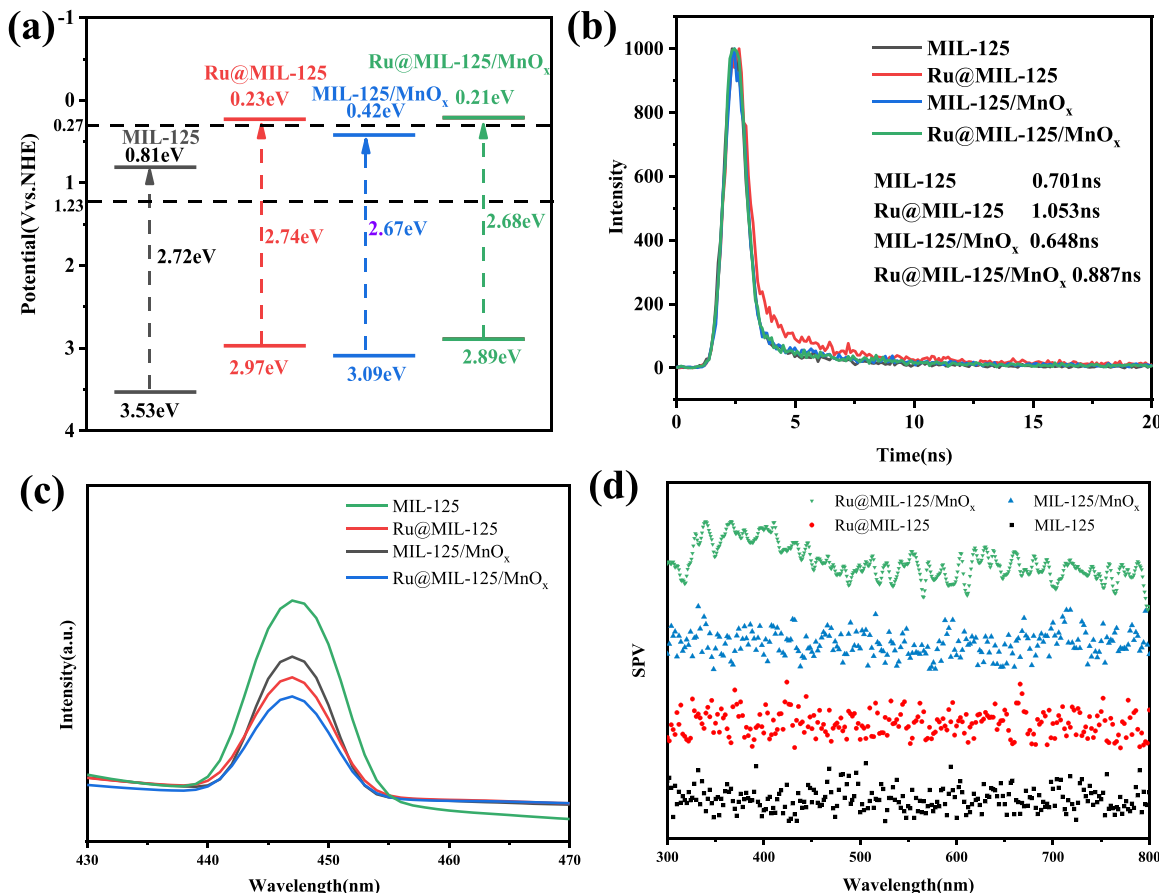


Fig. 6. (a) band structures of MIL-125, Ru@MIL-125, MIL-125/MnO_x and Ru@MIL-125/MnO_x, (b) transient fluorescence spectrum at room temperature, (c) steady state PL spectrum of the catalyst, and (d) surface optical voltage spectrum of the catalyst.

in Fig. 6c. After loaded with Ru and MnO_x , the fluorescence intensity of the sample decreased obviously, among which the composite sample Ru@MIL-125/ MnO_x has the lowest fluorescence intensity. The decrease of fluorescence intensity can be explained by the transfer of photo-generated electrons from the CB of MIL-125 to Ru and the transfer of photogenerated holes from the VB of MIL-125 to MnO_x , respectively, which reflected the lower recombination rate of the photogenerated carriers. That is, the sample has higher carrier separation efficiency, which is consistent with the results of transient fluorescence lifetime test. Fig. 6d shows the test results of Surface Photovoltage Spectroscopy (SPV). The surface potential was detected after the separation of photogenerated electrons and holes, so it can reflect the degree of photogenerated carrier separation. In MIL-125, Ru@MIL-125, MIL-125/ MnO_x , the potential difference is not obvious. In Ru@MIL-125/ MnO_x , obvious potential difference is observed in the light range of 300–450 nm. It can be inferred that photogenerated electrons and holes transfer to Ru and MnO_x respectively to promote the separation of photogenerated carriers. Therefore, it can be considered that the combination of Ru and MnO_x can enhance the separation of photogenerated carriers, thus increasing the concentration of carriers, which is ultimately reflected in the increase of photocatalytic nitrogen fixation activity.

The sample was tested by potentiometric titration. The volume of NaOH solution was taken as the horizontal axis, and the pH value of the measured solution and the calculated first derivative $d\text{pH}/dV$ were taken as the vertical axis. The results are shown in Fig. S10. According to the $d\text{pH}/dV$ -V curve (red curve in the figure), MIL-125 and Ru@MIL-125 samples have only one peak, while MIL-125/ MnO_x and Ru@MIL-125/ MnO_x samples after loading MnO_x have two peaks. Therefore, there is only one pKa value for MIL-125 and Ru@MIL-125, which are

calculated to be 3.95 and 3.99 respectively and are assigned to the titration of Ti-OH. MIL-125/ MnO_x and Ru@MIL-125/ MnO_x have pKa1 and pKa2 values. The pKa1 and pKa2 values of MIL-125/ MnO_x are 3.79 and 6.74, respectively, and the pKa1 and pKa2 values of Ru@MIL-125/ MnO_x are 3.74 and 6.62, respectively. The two pKa values are attributed to the titration of Ti-OH and Mn-OH respectively. The structural formula of NH₂-MIL-125 is $\text{Ti}_8\text{O}_8(\mu_2\text{-OH})_4(\text{C}_6\text{H}_3\text{C}_2\text{O}_4\text{NH}_2)_6$. In NH₂-MIL-125, there exists bridging hydroxyl $\mu_2\text{-OH}$, which is connected between two Ti atoms. The protonation of the hydroxyl-bridging $\mu_2\text{-OH}$ is involved in the titration, which causes a sudden jump in the titration curve with a pKa value of approximately 3.9. The protonation of the Mn-OH in MnO_x is involved in the titration with a pKa value of approximately 6.6.

3.4. Photocatalytic nitrogen fixation performance

Photocatalytic nitrogen fixation experiments were conducted on MIL-125, Ru@MIL-125, MIL-125/ MnO_x and Ru@MIL-125/ MnO_x respectively, and the indophenol blue method was used to detect NH_4^+ concentration after 2 h illumination to evaluate the nitrogen fixation activity of the samples, as shown in Fig. 7a. The standard curve is shown in Fig. S11. The activity of MIL-125 is very low, while after adding Ru or MnO_x , the activity is significantly improved, among which the composite catalyst Ru@MIL-125/ MnO_x has the highest photocatalytic activity, and the yield can reach 10.43 $\mu\text{mol/g/h}$. In addition, photocatalytic nitrogen fixation cycle test was carried out on Ru@MIL-125/ MnO_x to detect the stability of the catalyst, as shown in Fig. 7b. After three cycles, the photocatalytic activity remains stable, indicating that the composite catalyst Ru@MIL-125/ MnO_x has good stability. At the same time, it is calculated that the AQE of Ru@MIL-125/ MnO_x catalyst is 0.17% under the irradiation of monochromatic light at

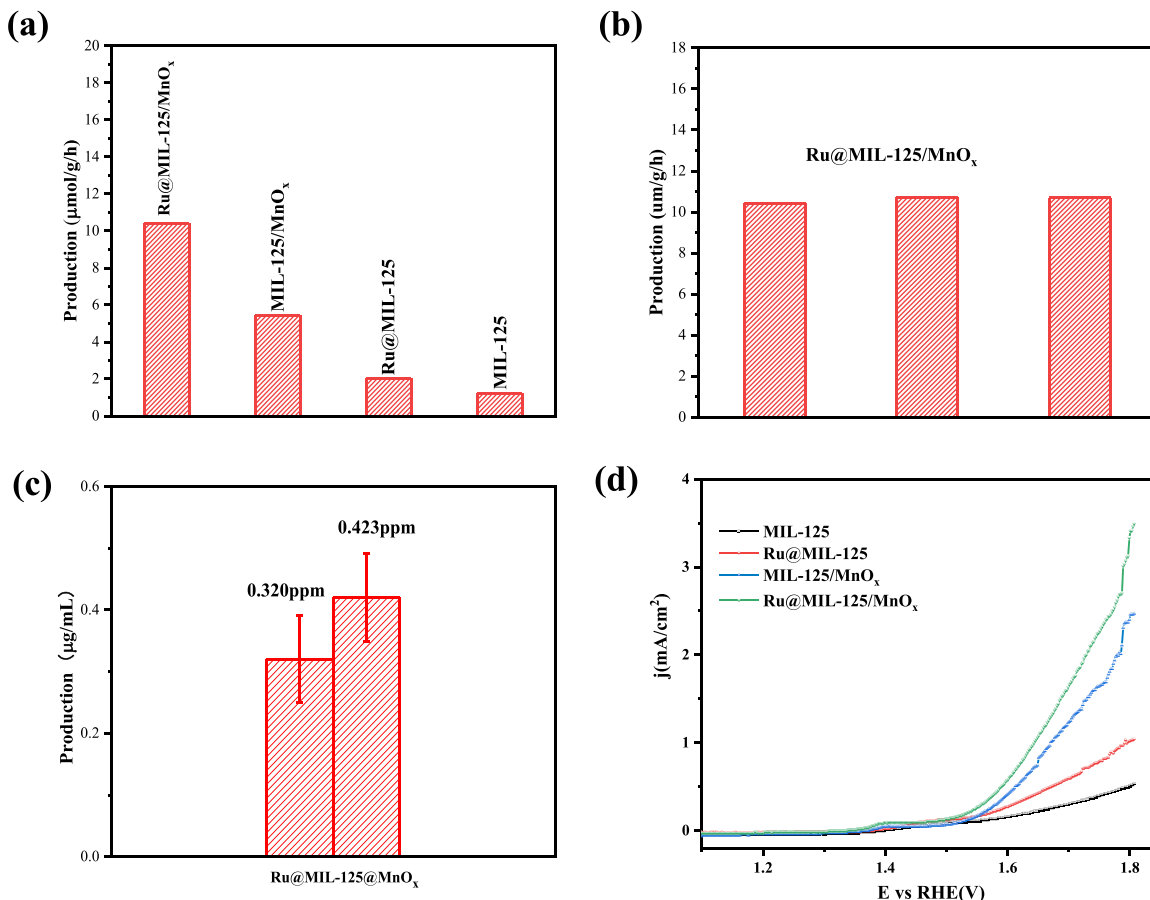


Fig. 7. (a) visible light-nitrogen fixation activity of the different catalysts, (b) cycle test activity of Ru@MIL-125/ MnO_x , (c) NH_4^+ concentration of Ru@MIL-125/ MnO_x solution by ion chromatography, and (d) OER polarization curves.

500 nm wavelength, which is higher than the previous work of Nano-SH-MOF@Self-Assembling Hollow Spherical g-C₃N₄(0.12%) [57]. We compared the results of AQE and photocatalytic activity with the previous reports, and the results are shown in Tables S3 and S4.

In order to further confirm the activity of the composite catalyst Ru@MIL-125/MnO_x and avoid the interference of errors, ion chromatography (Metrohm Eco IC) was used to detect NH₄⁺ concentration. The results are shown in Fig. 7c with the highest and average result of 0.423 and 0.372 ppm. The working curve of ion chromatography is shown in Fig. S12. The catalyst Ru@MIL-125/MnO_x was active in both tests, thus confirming the presence of NH₄⁺ in the solution after exposure to light.

The OER performance of the four catalysts were carried out in 1 M KOH, and the results were shown in Fig. 7d. Under the same current density, Ru@MIL-125/MnO_x and MIL-125/MnO_x showed a lower overpotential after the introduction of MnO_x, which indicated that MnO_x was the active site of oxygen production.

Since the source of NH₄⁺ in the solution may come from the environment or be decomposed by the catalyst, isotope calibration experiments were needed to verify that the N in NH₄⁺ came from nitrogen. Fig. 8a and b show the nitrogen fixation results under ¹⁴N₂ and ¹⁵N₂ atmosphere respectively. It can be seen that the ¹⁴N₂ sample detected very little ¹⁵N₂ indophenol blue with a molecular weight of 199, but the ¹⁵N₂ sample showed a significant increase in the proportion of the substance with a molecular weight of 199. Therefore, it can be determined that NH₄⁺ is generated by the reaction of nitrogen and water with the photocatalyst.

In order to study the stability of Ru@MIL-125/MnO_x, XRD, FT-IR, TEM and XPS characterizations were performed (Figs. S13 and S14 and Figs. S15 and S16). TEM images show that the appearance of the Ru@MIL-125/MnO_x did not change after reaction, and Ru nanoparticles with a size of about 5 nm ($d_{101} = 0.2087$ nm) and MnO_x nanoparticles with a size of about 5 nm ($d = 0.3427$ nm) were also observed after reaction. XRD and FT-IR results show that the crystal structure of the Ru@MIL-125/MnO_x was not destroyed before and after the reaction. XPS results show that the binding energy of the corresponding Ti element did not change after the reaction, while Mn element shows higher Mn⁴⁺/Mn³⁺ ratio after photocatalytic reaction. This result also indicates that MnO_x acts as the active sites of OER and the produced oxygen partially oxidized Mn³⁺ to Mn⁴⁺.

3.5. DFT calculation investigation

The electronic structure of MIL-125 is expected to be changed by introducing of Ru and MnO_x, which is closely related to nitrogen fixation

activity. Thus the total state densities (DOS) of Ru@MIL-125 and MIL-125/MnO_x were calculated using DFT. Fig. 9a shows the crystal structure models of Ru@MIL-125 and MIL-125/MnO_x by the DFT calculations. One Ru single atom and one MnO₂ molecule are suggest to bond with MIL-125, respectively. Fig. 9b revealed a bandgap of pure MIL-125 of about 3 eV between the VB edge (mainly composed of O2p orbitals) and the CB edge (mainly composed of Ti3d orbitals). After adding Ru and MnO_x, discrete energy levels lying in the band gap were formed, which is favorable for the absorption of visible light and thus improving the photocatalytic activity. Meanwhile, Gibbs free energy is also an influential factor in photocatalytic reaction (Fig. 9c). Hydrogenation of adsorbed nitrogen on Ru@MIL-125 and oxygen evolution reaction on MIL-125/MnO_x are used as the whole nitrogen fixation mechanism. For the half-reaction of N₂ reduction, the hydrogenation step leading to the formation of NNH* is considered as the rate-determining step. When N₂ molecule and H atom are adsorbed on Ru@MIL-125, it only needs to cross a energy barrier of 0.45 eV (the free energy changes from -1.31 to -0.86 eV) to form NNH*, which is very conducive for N₂ reduction. For the half-reaction of oxygen evolution reaction, when H₂O is adsorbed on MIL-125/MnO_x, it needs to cross a energy barrier of 1.10 eV (the free energy changes from -1.10 to 0 eV) to form hydroxy radicals-OH, this OER half-reaction is also relatively easy to happen. The DFT results explained that the addition of Ru and MnO_x in MIL-125 lowered the reaction energy barrier, thus promoting the photocatalytic activity.

4. Conclusion

NH₂-MIL-125 loaded with Ru was synthesized by hydrothermal method, and then combined with MnO_x by photodeposition to obtain composite catalyst Ru@MIL-125/MnO_x. The sample was characterized by various means and tested its activity through photocatalytic nitrogen fixation experiment. It was proved that the structure of MIL-125 was not destroyed in the composite sample, and it successfully formed Mn-O-Ti chemical bond with MnO_x. Electrochemical performance tests such as photocurrent and impedance indicate that Ru@MIL-125/MnO_x composite can increase the concentration of photogenerated carrier and enhance the photocatalytic activity. Fluorescence results show that Ru@MIL-125/MnO_x shows prolonged lifetime compared with pure MIL-125 and can reduce the recombination rate of photogenerated carrier. Through potentiometric titration experiment, it is found that Ru@MIL-125/MnO_x has two kinds of protons for Ti-OH and Mn-OH. The band structure was obtained by the determination of XPS valence band spectrum and UV-vis. Ru and MnO_x was successfully deposited on MIL-125 as the active sites of nitrogen reduction and OER respectively, thus a

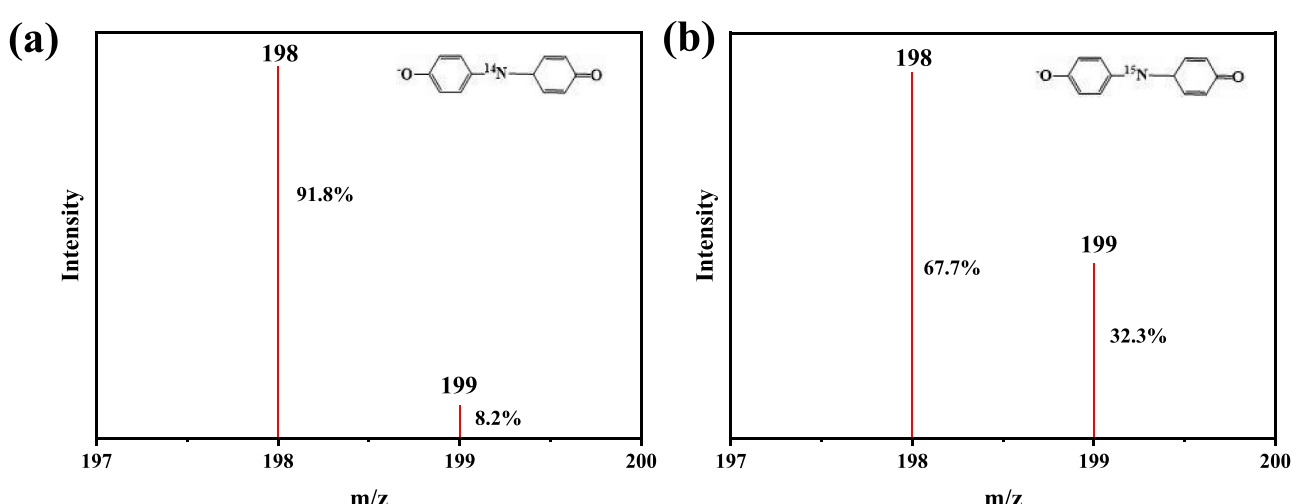


Fig. 8. (a) Results of indophenol blue mass spectroscopy prepared from ¹⁴N₂ using Ru@MIL-125/MnO_x, (b) results of indophenol blue prepared from ¹⁵N₂ using Ru@MIL-125/MnO_x.

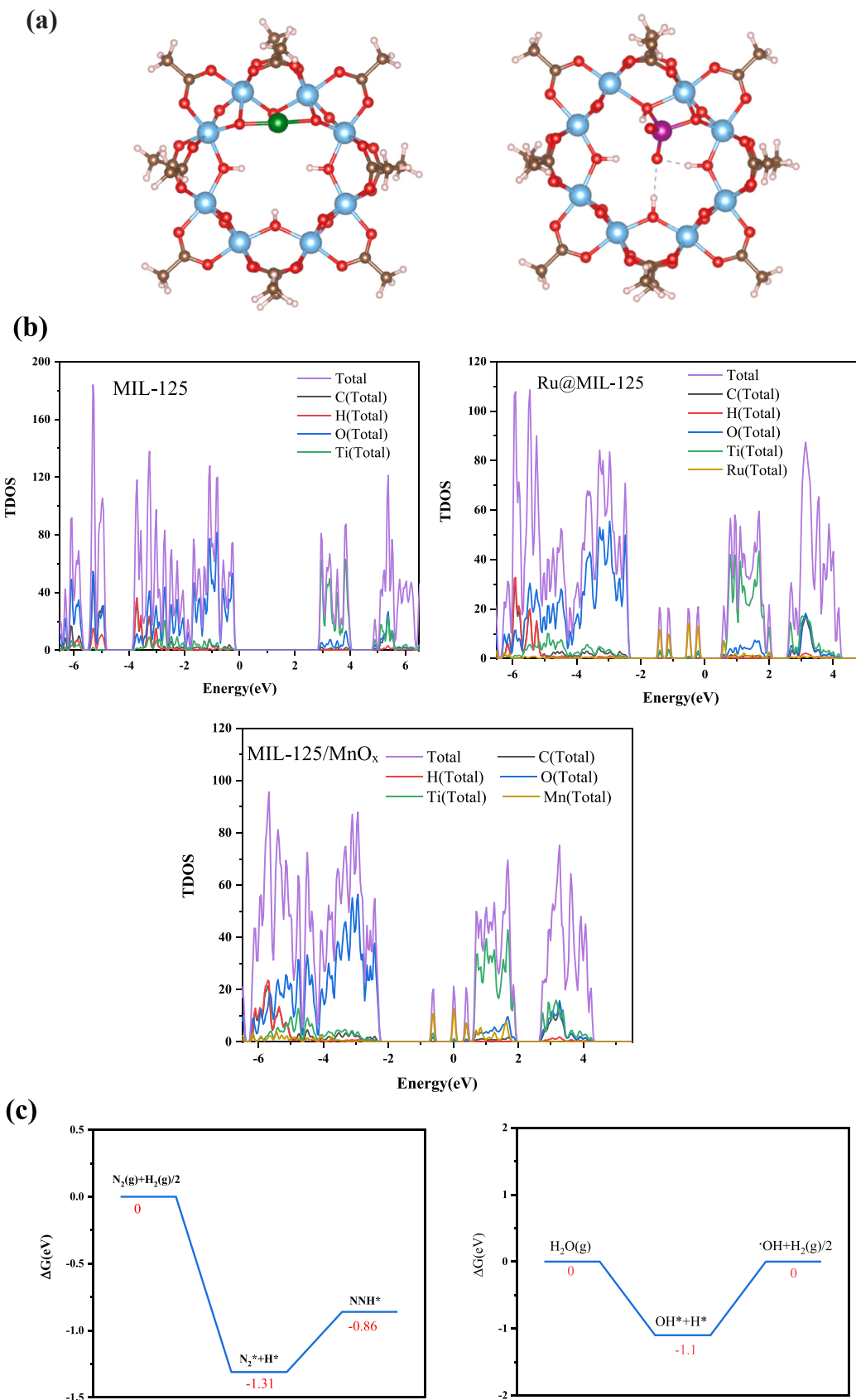


Fig. 9. (a) Diagram of the atomic structure of Ru@MIL-125 and MIL-125/MnO_x (Atomic color: pink, H; brown, C; blue, Ti; red, O; purple, Mn; green, Ru), (b) Calculated total density of states for MIL-125, Ru@MIL-125 and MIL-125/MnO_x, (c) Calculated free energy diagram for N₂ fixation on Ru@MIL-125 and oxygen evolution reaction on MIL-125/MnO_x, respectively.

composite photocatalyst Ru@MIL-125/MnO_x with good nitrogen fixing activity was obtained. The DFT results showed that the introduction of Ru and MnO_x in MIL-125 reduced the reaction energy barrier of nitrogen reduction and OER, thus improving the photocatalytic activity of nitrogen fixation. These results provide clear ideas for the design of nitrogen fixation cocatalysts through combining nitrogen reduction and OER active sites together.

CRediT authorship contribution statement

Wang Chuanjiao: Conceptualization, Data curation, Formal analysis, Investigation, Methodology, Writing – original draft, Writing – review & editing. **Wang Shuo:** Data curation, Formal analysis, Writing – original draft. **Wang Danhong:** Conceptualization, Data curation, Formal analysis, Funding acquisition, Investigation, Methodology, Resources, Validation, Writing – original draft, Writing – review & editing. **Bu Xianhe:** Conceptualization, Data curation, Formal analysis, Funding acquisition, Investigation, Methodology, Supervision, Writing – original draft, Writing – review & editing. **Ping Yi:** Data curation, Formal analysis. **Zhao Zhe:** Data curation, Writing – original draft. **Guo Dongxue:** Formal analysis, Writing – original draft.

Declaration of Competing Interest

All authors declare that they have no known conflicts of interest that could affect the work reported in this paper.

Data availability

Data will be made available on request.

Acknowledgements

This work was supported by the 111 project (B18030) from China and the National Natural Science Foundation of China (22372082). The authors acknowledge the financial support by Haihe Laboratory of Sustainable Chemical Transformations (NO. YYJC202101).

Appendix A. Supporting information

Supplementary data associated with this article can be found in the online version at doi:10.1016/j.apcatb.2024.123781.

References

- [1] T. Spatzl, K.A. Perez, O. Einsle, J.B. Howard, D.C. Rees, Ligand binding to the FeMo-cofactor: structures of CO-bound and reactivated nitrogenase, *Science* (2014).
- [2] Z. Li, Y. Qu, K. Hu, M. Humayun, S. Chen, L. Jing, Improved photoelectrocatalytic activities of BiOCl with high stability for water oxidation and MO degradation by coupling RGO and modifying phosphate groups to prolong carrier lifetime, *Appl. Catal. B Environ.* (2016).
- [3] C.J.M. van der Ham, M.T.M. Koper, D.G.H. Hetterscheid, Challenges in reduction of dinitrogen by proton and electron transfer, *Chem. Soc. Rev.* (2014).
- [4] B.M. Hoffman, D. Lukoyanov, Z.-Y. Yang, D.R. Dean, L.C. Seefeldt, Mechanism of nitrogen fixation by nitrogenase: the next stage, *Chem. Rev.* (2014).
- [5] C. Xiao, L. Zhang, K. Wang, H. Wang, Y. Zhou, W. Wang, A new approach to enhance photocatalytic nitrogen fixation performance via phosphate-bridge: a case study of SiW12/K-C3N4, *Appl. Catal. B Environ.* (2018).
- [6] L. Buzzetti, G.E.M. Crisenzia, P. Melchiorre, Mechanistic studies in photocatalysis, *Angew. Chem. Int. Ed.* (2019).
- [7] J. Gallagher, Photocatalysis: into the dark, *Nat. Energy* (2017).
- [8] C. Xu, P. Ravi Anusuyadevi, C. Aymonier, R. Luque, S. Marre, Nanostructured materials for photocatalysis, *Chem. Soc. Rev.* (2019).
- [9] Y.-H. Liu, C.A. Fernández, S.A. Varanasi, N.N. Bui, L. Song, M.C. Hatzell, Prospects for aerobic photocatalytic nitrogen fixation, *ACS Energy Lett.* (2021).
- [10] D. Dong, C. Yan, J. Huang, N. Lu, P. Wu, J. Wang, Z. Zhang, An electron-donating strategy to guide the construction of MOF photocatalysts toward co-catalyst-free highly efficient photocatalytic H₂ evolution†, *J. Mater. Chem. A* (2019).
- [11] Y.H. Zhuang Xiong, Rusheng Yuan, Zhengxin Ding, Wee-Jun Ong, Sibo Wang, Hollow NiCo₂S₄ nanospheres as a cocatalyst to support zincox₂s₄ nanosheets for visible-light-driven hydrogen production, *Acta Phys. -Chim. Sin.* 38 (2022) 2111021 (-).
- [12] J.D. Xiao, Q. Shang, Y. Xiong, Q. Zhang, Y. Luo, S.H. Yu, H.L. Jiang, Boosting Photocatalytic Hydrogen Production of a Metal–Organic Framework Decorated with Platinum Nanoparticles: The Platinum Location Matters, *Angewandte Chemie International Edition*, 2016.
- [13] Y.-Z. Chen, Z.U. Wang, H. Wang, J. Lu, S.-H. Yu, H.-L. Jiang, Singlet oxygen-engaged selective photo-oxidation over Pt nanocrystals/porphyrinic MOF: the roles of photothermal effect and Pt electronic state, *J. Am. Chem. Soc.* (2017).
- [14] J.-D. Xiao, L. Han, J. Luo, S.-H. Yu, H.-L. Jiang, Back cover: integration of plasmonic effects and Schottky junctions into metal–organic framework composites: steering charge flow for enhanced visible-light photocatalysis, *Angew. Chem. Int. Ed.* (2018).
- [15] D. Li, S.-H. Yu, H.-L. Jiang, From UV to near-infrared light-responsive metal–organic framework composites: plasmon and upconversion enhanced photocatalysis, *Adv. Mater.* (2018).
- [16] H. Jia, N. Yao, J. Zhu, Y. Liu, Y. Lao, H. Cong, W. Luo, Ni3N modified MOF heterostructure with tailored electronic structure for efficient overall water splitting, *Chin. J. Struct. Chem.* (2022).
- [17] S. Yangyang, J. Houqiang, S. Yanjun, Z. Guangxun, Z. Huijie, C. Shuai, L. Sixiao, Z. Lei, L. Wenting, Z. Xingwang, P. Huan, Synergistic effect of oxygen vacancy and high porosity of nano MIL-125(Ti) for enhanced photocatalytic nitrogen fixation, *Angew. Chem. Int. Ed.* (2023).
- [18] L. Xiao-Hong, L. Hui, J. Shen-Long, Y. Lan, L. Hui-Yi, L. Qi-Long, B. Wei, Z. Qun, X. Chong, X. Yi, Constructing mimic-enzyme catalyst: polyoxometalates regulating carrier dynamics of metal–organic frameworks to promote photocatalytic nitrogen fixation, *ACS Catal.* (2023).
- [19] Y. Fu, K. Zhang, Y. Zhang, Y. Cong, Q. Wang, Fabrication of visible-light-active MR/NH₂-MIL-125(Ti) homojunction with boosted photocatalytic performance, *Chem. Eng. J.* (2021).
- [20] L. Ya, W. Zhenkang, J. Haoqing, Z. Lifang, Q. Tao, Y. Chenglin, L. Jianmei, Excluding false positives: perspective toward credible ammonia quantification in nitrogen reduction reaction, *Chin. J. Catal.* (2022).
- [21] Q. Xiu, W. Yanjiao, S. Mengjie, H. Ye, Z. Xiaoli, T. Jian, S. Minhua, Heterostructuring 2D TiO₂ nanosheets in situ grown on Ti3C2Tx MXene to improve the electrocatalytic nitrogen reduction, *Chin. J. Catal.* (2022).
- [22] D. Dapeng, T. Xueqin, W. Pengyan, W. Jian, H. Jindou, Z. Haiyan, L. Dedi, Z. Zhenyi, An anthracene-9-carboxylic acid-based [Cu₂O] cluster templated by a bromine anion for heterogeneous catalytic chemical fixation of carbon dioxide, *J. Mater. Chem. A* (2022).
- [23] H. Kim, A. Jan, D.-H. Kwon, H.-I. Ji, K.J. Yoon, J.-H. Lee, Y. Jun, J.-W. Son, S. Yang, Exsolution of Ru nanoparticles on BaCe_{0.9}Y_{0.1}O₃ modifying geometry and electronic structure of Ru for ammonia synthesis reaction under mild conditions, *Small* (2022).
- [24] F. Zhou, C. Sun, Nitrate-to-ammonia conversion on Ru/Ni hydroxide hybrid through zinc-nitrate fuel cell, *Small* (2022).
- [25] M. Kitano, Y. Inoue, M. Sasase, K. Kishida, Y. Kobayashi, K. Nishiyama, T. Tada, S. Kawamura, T. Yokoyama, M. Hara, H. Hosono, Self-organized Ruthenium–Barium Core–Shell Nanoparticles on a Mesoporous Calcium Amide Matrix for Efficient Low-Temperature Ammonia Synthesis, *Angew. Chem. Int. Ed.* (2018).
- [26] S. Wang, D. Guo, M. Zong, C. Fan, X. Jun, D.-H. Wang, Unravelling the strong metal-support interaction between Ru quantum dots and g-C₃N₄ for visible-light photocatalytic nitrogen fixation, *Appl. Catal. A: Gen.* (2021).
- [27] A. Awati, H. Maimaiti, S. Wang, B. Xu, Photo-derived fixation of dinitrogen into ammonia at ambient condition with water on ruthenium/coal-based carbon nanosheets, *Sci. Total Environ.* (2019).
- [28] Y. Xue, Z.S. Fishman, J.A. Röhr, Z. Pan, Y. Wang, C. Zhang, S. Zheng, Y. Zhang, S. Hu, Tunable nano-interfaces between MnO_x and layered double hydroxides boost oxygen evolving electrocatalysis†, *J. Mater. Chem. A* (2018).
- [29] J.G. Vos, T.A. Wezendonk, A.W. Jeremiassie, M.T.M. Koper, MnO_x/IrO_x as selective oxygen evolution electrocatalyst in acidic chloride solution, *J. Am. Chem. Soc.* (2018).
- [30] Z. Jin, A.J. Bard, Surface interrogation of electrodeposited MnO_x and CaMnO₃ perovskites by scanning electrochemical microscopy: probing active sites and kinetics for the oxygen evolution reaction, *Angew. Chem. Int. Ed.* (2020).
- [31] Z. Liu, Z. Zhao, W. Zhang, Y. Huang, Y. Liu, D. Wu, L. Wang, S. Chou, Toward high-performance lithium–oxygen batteries with cobalt-based transition metal oxide catalysts: advanced strategies and mechanical insights, *InfoMat* (2021).
- [32] K. Shen, S. Kumari, Y.-C. Huang, J. Jang, P. Sautet, C.G. Morales-Guio, Electrochemical oxidation of methane to methanol on electrodeposited transition metal oxides, *J. Am. Chem. Soc.* (2023).
- [33] G. Xu, J. Ma, L. Wang, W. Xie, J. Liu, Y. Yu, H. He, Insight into the origin of sulfur tolerance of Ag/Al₂O₃ in the H₂-C3H₆-SCR of NO_x, *Appl. Catal. B Environ.* (2018).
- [34] B. Zhang, J. Ji, B. Liu, D. Zhang, S. Liu, H. Huang, Highly efficient ozone decomposition against harsh environments over long-term stable amorphous MnO_x catalysts, *Appl. Catal. B: Environ.* (2022).
- [35] F. Raziq, L. Sun, Y. Wang, X. Zhang, M. Humayun, S. Ali, L. Bai, Y. Qu, H. Yu, L. Jing, Synthesis of large surface-area g-C₃N₄ comodified with MnO_x and Au-TiO₂ as efficient visible-light photocatalysts for fuel production, *Adv. Energy Mater.* (2017).
- [36] P. Martínez-Zarza, J.M. Arrieta, M.C. Muñoz-Roca, P. Gili, Synthesis and characterization of new octamolybdates containing imidazole, 1-methyl- or 2-methyl-imidazole co-ordinatively bound to molybdenum, *J. Chem. Soc. Dalton Trans.* (1993) 1551–1557.

- [37] X. Zhang, Z. Chen, Y. Luo, X. Han, Q. Jiang, T. Zhou, H. Yang, J. Hu, Construction of NH₂-MIL-125(Ti)/Cds Z-scheme heterojunction for efficient photocatalytic H₂ evolution, *J. Hazard. Mater.* (2020).
- [38] F. Mohammadnezhad, S. Kampouri, S.K. Wolff, Y. Xu, M. Feyzi, J.-H. Lee, X. Ji, K. C. Stylianou, Tuning the Optoelectronic Properties of Hybrid Functionalized MIL-125-NH₂ for photocatalytic hydrogen evolution, *ACS Appl. Mater. Interfaces* (2021).
- [39] G. Kresse, J. Furthmüller, Efficient iterative schemes for ab initio total-energy calculations using a plane-wave basis set, *Phys. Rev. B* (1996).
- [40] G. Kresse, J. Furthmüller, Efficiency of ab-initio total energy calculations for metals and semiconductors using a plane-wave basis set, *Comput. Mater. Sci.* 6 (1996) 15–50.
- [41] N. Perdew, N. Burke, N. Ernzerhof, Generalized gradient approximation made simple, *Phys. Rev. Lett.* (1996).
- [42] S. Grimme, J. Antony, S. Ehrlich, H. Krieg, A consistent and accurate ab initio parametrization of density functional dispersion correction (DFT-D) for the 94 elements H-Pu, *J. Chem. Phys.* (2010).
- [43] M.A. Nasalevich, R. Becker, E.V. Ramos-Fernandez, S. Castellanos, S.L. Veber, M. V. Fedin, F. Kapteijn, J.N.H. Reek, J.I. van der Vlugt, J. Gascon, Co@NH₂-MIL-125 (Ti): cobaloxime-derived metal–organic framework-based composite for light-driven H₂ production†, *Energy Environ. Sci.* (2014).
- [44] Y. Fu, L. Sun, H. Yang, L. Xu, F. Zhang, W. Zhu, Visible-light-induced aerobic photocatalytic oxidation of aromatic alcohols to aldehydes over Ni-doped NH₂-MIL-125(Ti), *Appl. Catal. B Environ.* (2016).
- [45] P. Putthiaraj, W.-S. Ahn, Highly active palladium nanoparticles immobilized on NH₂-MIL-125 as efficient and recyclable catalysts for Suzuki–Miyaura cross coupling reaction, *Catal. Commun.* (2015).
- [46] Y. Fu, D. Sun, Y. Chen, R. Huang, Z. Ding, X. Fu, Z. Li, An amine-functionalized titanium metal–organic framework photocatalyst with visible-light-induced activity for CO₂ Reduction†, *Angew. Chem.* (2012).
- [47] I. Ahmed, S.H. Jhung, Effective adsorptive removal of indole from model fuel using a metal–organic framework functionalized with amino groups, *J. Hazard. Mater.* (2014).
- [48] G. Wen, Z. Guo, Facile modification of NH 2 -MIL-125(Ti) to enhance water stability for efficient adsorptive removal of crystal violet from aqueous solution, *Colloids Surf. A Physicochem. Eng. Asp.* (2018).
- [49] R. Bibi, L. Wei, Q. Shen, W. Tian, O. Oderinde, N. Li, J. Zhou, Effect of amino functionality on the uptake of cationic dye by titanium-based metal organic frameworks, *J. Chem. Eng. Data* (2017).
- [50] G. Zhou, M.-F. Wu, Q.-J. Xing, F. Li, H. Liu, X.-B. Luo, J.-P. Zou, J.-M. Luo, A.-Q. Zhang, Synthesis and characterizations of metal-free Semiconductor/MOFs with good stability and high photocatalytic activity for H₂ evolution: A novel Z-Scheme heterostructured photocatalyst formed by covalent bonds, *Appl. Catal. B Environ.* (2017).
- [51] S. Daliran, A. Santiago-Portillo, S. Navalón, A.R. Oveisi, M. Álvaro, R. Ghorbani-Vaghei, D. Azarifar, H. García, Cu(II)-Schiff base covalently anchored to MIL-125 (Ti)-NH₂ as heterogeneous catalyst for oxidation reactions, *J. Colloid Interface Sci.* (2018).
- [52] H.E. Emam, R.M. Abdelhameed, Anti-UV radiation textiles designed by embracing with Nano-MIL (Ti, In)–metal organic framework, *ACS Appl. Mater. Interfaces* (2017).
- [53] Y. Ling, Z. Chaoqi, Z. Yingying, B. Tong, W. Jing, T. Cheng, D. Ajun, Y. Chengzhong, L. Chao, A S-Scheme MOF-on-MOF heterostructure, *Adv. Funct. Mater.* (2023).
- [54] J. Haopeng, W. Lele, Y. Xiaohui, S. Lijuan, L. Jinhe, Y. Juan, L. Qinjin, Precise regulation of built-in electric field over NH₂-MIL-125-Ti/WO₃-x S-scheme heterojunction for achieving simultaneous formation of CO and H₂O₂ from CO₂ and H₂O, *Chem. Eng. J.* (2023).
- [55] F. Yangjie, T. Meng, G. Zhonglu, H. Derek, X. Youran, D. Hao, Z. Chao, G. Jiayun, L. Qiang, W. Qi, Fabrication of wide-spectra-responsive NA/NH₂-MIL-125(Ti) with boosted activity for Cr(VI) reduction and antibacterial effects, *Chem. Eng. J.* (2022).
- [56] Z. Baofang, Z. Ziyu, L. Wenting, Z. Meijin, P. Yunhong, W. Tiejun, Confinement of Cu₂O by in-situ derived NH₂-MIL-125@TiO₂ for synergistic photothermal-driven hydrogen evolution from aqueous-phase methanol reforming, *Chem. Eng. J.* (2023).
- [57] D. Zhu, W. Shuo, Y. Sai, Z. Yu-Jia, W. Dan-Hong, Nano-SH-MOF@self-assembling hollow spherical g-C₃N₄ heterojunction for visible-light photocatalytic nitrogen fixation, *ChemCatChem* (2023).